Strojnícky časopis – *Journal of* MECHANICAL ENGINEERING,
VOL 74 (2024), NO 3, 15 - 26

NUMERICAL INVESTIGATION OF THE CRITICAL AREAS OF THE FREIGHT TRAIN WHEEL WEB

DLHÝ Pavol[1, *], PETER Ondřej[2], FAJKOŠ Rostislav[2], POKORNÝ Pavel[1], HUTAŘ Pavel[1], JAMBOR Michal[1]

[1] *Institute of Physics of Materials of the Czech Academy of Sciences, v.v.i., Žižkova 513/22, Brno, Czech Republic*
[2] *BONATRANS GROUP a.s., Revoluční 1234, 735 94, Bohumín, Czech Republic*
**Corresponding author: dlhy@ipm.cz*

Abstract: This paper aims to investigate the impact of braking with brake blocks on the fatigue lifetime of the train wheel web. Braking generates heat, causing uneven thermal stress and residual stresses as it cools. This can lead to the initiation of fatigue cracks in the wheel web. Therefore, the main issue is the numerical modelling of the railway wheel loaded by mechanical and thermal loads. A complex fatigue investigation is proposed to validate the numerical models and determine critical areas of the wheel web where fatigue cracks can initiate.

KEYWORDS: Railway wheel, Fatigue, Numerical simulations

1 Introduction

Maintaining railway wheelsets is essential for ensuring safety, minimising maintenance expenses, and preserving the reliability of the railway system. In-use monitoring [1] and safe life design techniques can be used to maintain safety of a railway wheelset. As one of the train most heavily loaded components, the wheelset integrity is important for the safe operation of railways. Fig. 1 schematically describes the wheelset construction. During train operation, railway wheels suffer from frequent braking, leading to surface damage in the areas of rail-wheel contact [2–5]. Different treatments can be applied to prevent surface damage, e.g., induction hardening, which improves wear resistance [6]. However, damage is not only limited to these surface contact areas. Some cracks were revealed in the wheel web, see Fig. 2. So far, there is no explanation why fatigue cracks should initiate in the wheel web. Therefore, this paper investigates the wheel web area using thermal (thermal load from braking) and mechanical (load given by train weight and interaction of wheel and rail during train movement) simulations.

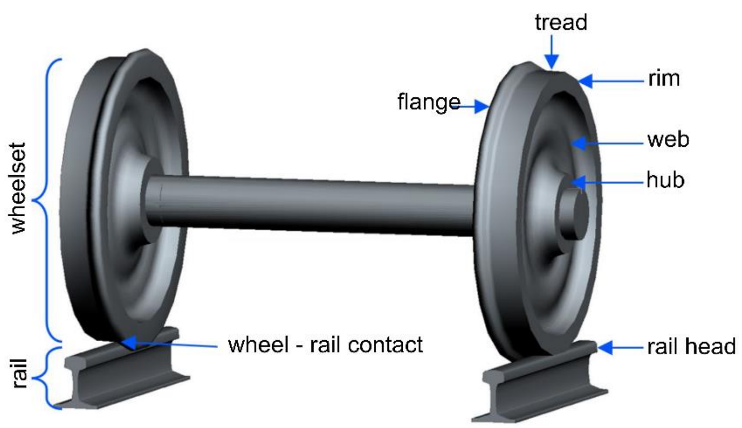

Fig. 1 Typical structure of a wheelset with marked names of the wheel parts [5]

DOI: 10.2478/scjme-2024-0030, Print ISSN 0039-2472, On-line ISSN 2450-5471

The wheel web profile is frequently designed as curved profile to counteract thermal expansion effects when the wheel heats up. Despite this precaution, these curvatures can act as stress concentrators and introduce additional bending loads on the wheel, potentially leading to areas susceptible to fatigue damage, particularly in the web area. Stress concentrators make the web a critical zone that requires careful consideration during the wheel design phase. Numerical simulations are utilised to address and mitigate these issues, allowing designers to identify and evaluate potential problematic areas within the web. By incorporating such simulations, designers can better predict and prevent fatigue crack initiation, ensuring the wheel integrity and long maintenance intervals. The wheel design standard EN 13979 [7] specifies solely the mechanical loadings a designed wheel should withstand, outlining three distinct loading scenarios based on the train motion: straight track, curved track, and turnout.

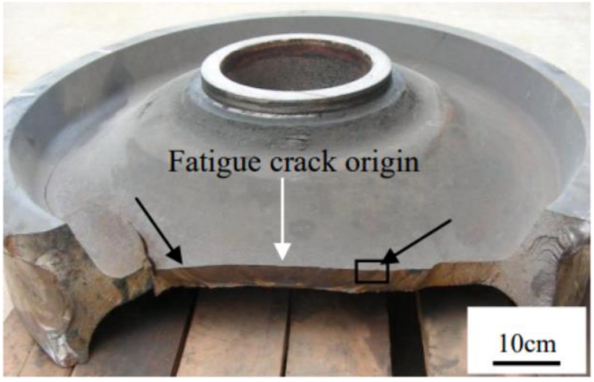

Fig. 2 Example of the wheel web fatigue crack initiation and wheel fracture [8, 9]

2 Material

The material of the railway wheel is low-alloy R73 steel, with the chemical composition shown in Table 1 [10]. Three different wheels were examined. The annealed wheel, standard hardened wheel, and standard hardened wheel after the braking test. The initial step in studying the mechanical properties was characterising the material in its basic state, free of residual stresses. A representative train wheel underwent annealing after the standard manufacturing process to ensure a uniform material structure without residual stresses. Structural analysis confirmed that normalisation annealing produced a homogeneous structure, preparing the material in its basic state for further analyses.

Table 1 Chemical composition (wt.%) of the R73 steel [10]

C	Mn	Si	P	S	Cu	Cr
0.51	0.75	0.3	0.012	0.009	0.08	0.24
Ni	O	H	Mo	V	N	AlC
0.16	1.8	1.2	0.04	0.003	0.0053	0.023

For the macrostructural analysis, 20 mm thick segments were cut from the examined wheels (Fig. 3). Further investigated areas, labelled 1 to 5, are shown as white-shaded regions in Fig. 3. These segments were ground and then immersed in an HCl + H_2O (1:1) bath for 24 hours to observe microstructure through the wheel cross-section. The analysis revealed no significant inhomogeneities or defects in the annealed and standard hardened wheel. However, in the wheel rim, a heat-affected zone was observed in the standard hardened wheel subjected to the braking test.

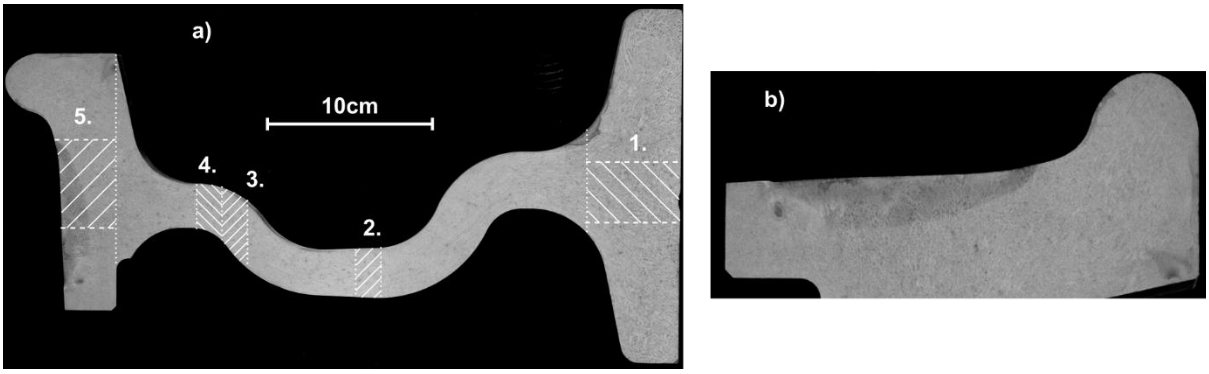

Fig. 3 Macroscopic image sections of the examined wheels. Marked are the sampling points for microstructural analysis (white-shaded areas). a) standard hardened wheel after braking test; b) detail of the macrostructure in the wheel rim area of the standard hardened wheel after braking test with visible heat affected zone.

Table 2 Comparison of the microstructure in selected locations in an annealed wheel, a standard hardened wheel, and a standard hardened wheel after the braking test

Area	Annealed wheel	Standard hardened wheel	Standard hardened wheel after the braking test
5 (close to the wheel-rail surface)	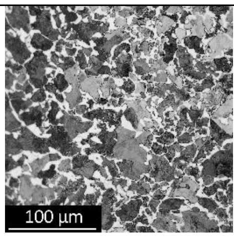	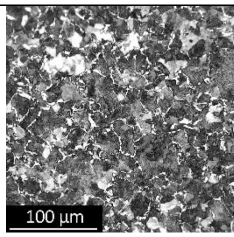	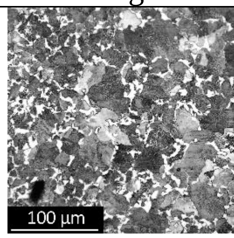
5 (approx. 12 mm under the surface)	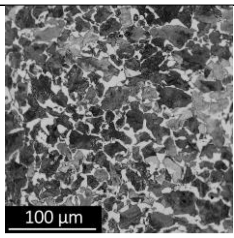	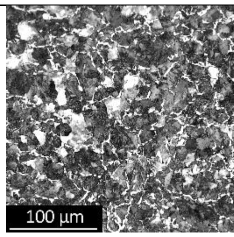	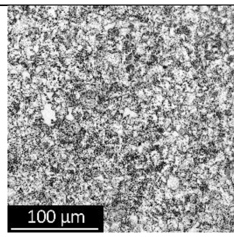
4	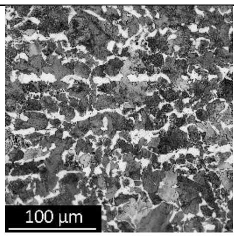	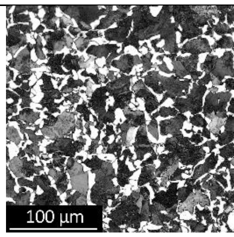	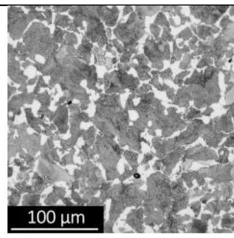
3	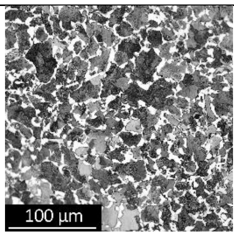	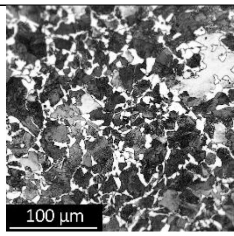	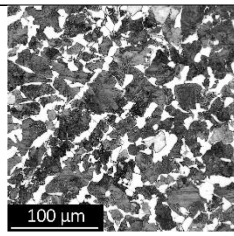

2	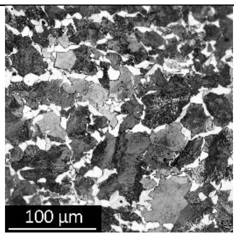	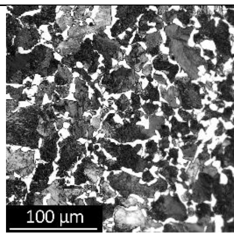	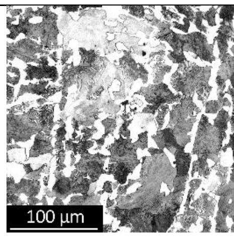
1	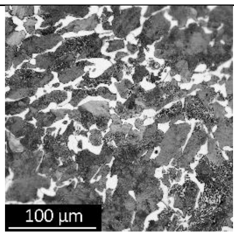	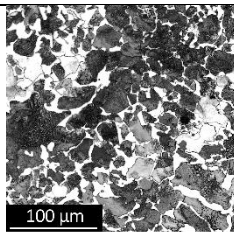	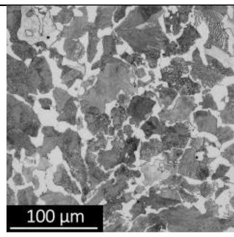

A comparison of the microstructure of the selected areas is shown in Table 2. Samples were taken from the locations marked in Fig. 3 and then prepared using standard procedures to prepare metallographic samples. The procedure consisted of grinding on SiC abrasive papers of different grits followed by mechanical polishing using diamond pastes. The samples were subsequently etched in 2% Nital solution (HNO_3 solution in ethanol) to highlight the microstructure. The actual observation was performed using an Olympus DSX 1000 digital light microscope.

The microstructure of the examined wheels consisted of a combination of lamellar pearlite and ferrite. In the standard hardened wheel, a slightly different morphology of lamellar pearlite was observed in the rim area (area 5 Fig. 3) due to the applied heat treatment. After the braking test, the standard hardened wheel showed significant microstructural changes in the rim area, particularly around 12 mm from the wheel-rail contact surface. In this region, the microstructure consisted of a mixture of ferrite and globular pearlite due to substantial spheroidization of the carbides. Apart from these differences in the rim area, no major changes in microstructure or significant defects were detected in the rest of the wheel cross-section.

3 The braking tests

The braking tests were conducted on a brake bench (see Fig. 4), where different braking scenarios can be simulated, such as regular stopping, emergency, and fallback braking. For freight wheels, the test simulates fallback braking, which involves a 45-minute braking cycle where the wheel is continuously braked at 50 kW of power while maintaining a simulated speed of 60 km/h. Note that a 45-minute braking test reflects the operational conditions of a freight train descending from mountains (e.g. Alps). The entire braking test consists of 10 repetitive braking and cooling cycles. The test results include an evaluation of parameters like axial deformation of the wheel rim, both when hot and after cooling down (at room temperature), which could influence the wheel derailment. The EN 13979 standard also commands the rim residual tangential (circumferential) stress determination using an ultrasonic method, which influences crack growth rate and initiation probability in the rim area. Determined values are then compared to the limits specified in the EN 13979 standard.

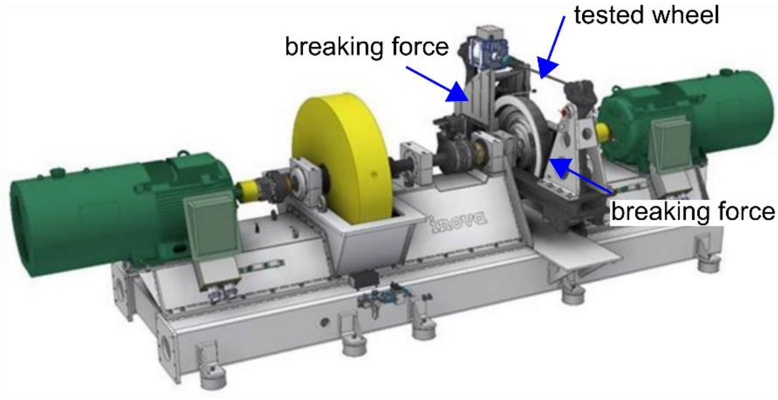

Fig. 4 3D model of a brake bench showing two motors, a flywheel and a tested wheel

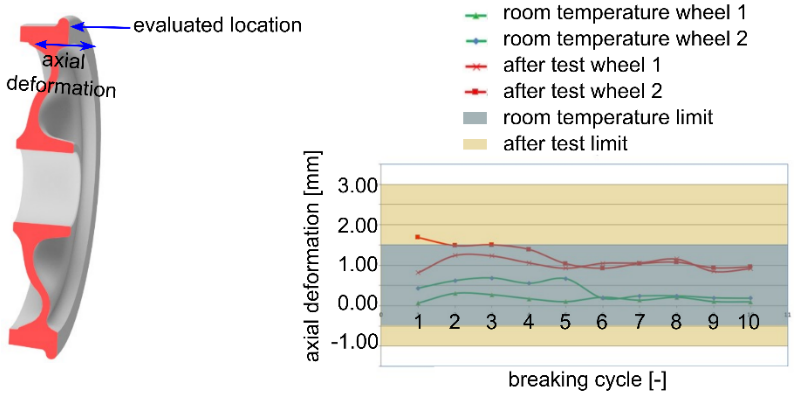

Fig. 5 Example of the axial deformation evaluation results for the two tested wheels

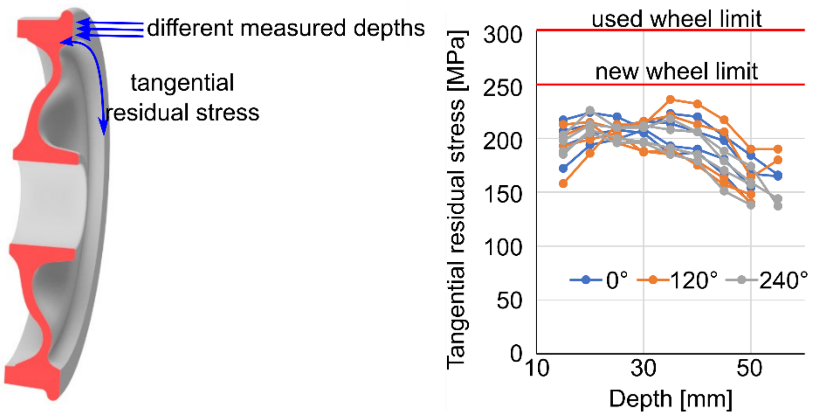

Fig. 6 Example of tangential residual stress evaluation results after the braking for the two tested wheels

Axial deformation is evaluated as the maximum difference between reference measurement and measurement after the braking cycle. The reference measurement is taken after the wheel is mounted to the brake bench. The dial indicator over the whole circumference measures axial deformation. Fig. 5 compares the limit values according to the EN 13979 standard and measured deformation on the wheel rim. The yellow area, see Fig. 5, corresponds to limits +3/-1 mm during and after the braking (for the hot wheel). The grey area corresponds to limits +1.5/-0.5 mm for the cooled wheel at room temperature. Lines describe the axial deformation of two tested wheels. Except for the first braking cycle, measured deflections are more or less steady during testing. Final axial deformation measured at room temperature (after cooling down) is generally lower compared to the deformations measured after the braking test (hot state). All measured deflections are within the limits set by the standard.

The ultrasound measurement technique determines the tangential residual stress. Different depths under the wheel-rail contact surface are measured. For each depth, three different angular positions with a spacing of 120° are considered. Fig. 6 shows determined residual stress with EN 13979 standard limits. Two different wheels were measured again. Solid red lines show limits for new (250 MPa average for one depth) or used (300 MPa average for one depth) wheels. Blue (0°), orange (120°), and grey (240°) lines represent the stress determined at different angular positions around the wheel circumference. All three angular positions follow a similar pattern, showing some variation but generally staying within the same range of stress. At shallower depths (10-30 mm), the stress levels for all three angles are around 200 MPa, see Fig. 6. As the determination depth increases beyond 30 mm, the stress gradually decreases for all three angles, falling to values around 150 MPa at 50 mm depth. All determined residual stresses are within the limits set by the standard.

4 Numerical modelling

To explore the issue of wheel fatigue, the numerical study follows the methodology outlined in EN 13979, which focuses solely on mechanical wheel loading and does not account for factors such as the temperature rise caused by braking. However, practical experience [5, 11, 12] has shown that railway wheel failures can occur. Thermal loading can lead to damage in both the wheel-rail contact area and the wheel web. This study aims explicitly to predict critical locations in the wheel web. Consequently, a new numerical approach has been developed, including the effects of braking-induced thermal loads.

Mechanical loading (according to EN 13979 standard) is defined as three different track types. Track types are straight track, curved track and turnout. The positions and calculations of the applied mechanical loads are detailed in Table 3. In this table, "Fz" and "Fy" represent the forces applied in the Z and Y axis directions, respectively, while "g" refers to the acceleration due to gravity. "Q" indicates the load per wheel, determined by the load capacity of the wheelset.

Table 3 Driving types according to EN 13979 standard

Track type	Straight track	Curved track	Turnout
Graphical representation of the position of the force acting on the wheel rim	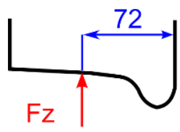	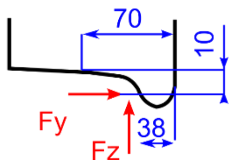	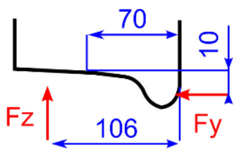
The formula for calculating the applied force	Fz = 1.25 * Q * g	Fz = 1.25 * Q * g Fy = 0.6 * Q * g	Fz = 1.25 * Q * g Fy = 0.36 * Q * g

Numerical simulations were carried out using ANSYS software, employing mechanical and thermal finite element models. The mechanical model was constructed with a symmetry plane, incorporating around 143,000 quadratic elements. It defined the material as isotropic and linearly elastic, characterised by a Poisson ratio of 0.3 and Young modulus of 206 GPa. Fig. 7 shows the boundary conditions for the mechanical model. External mechanical loading was set in several steps following the type of track being investigated, as specified in the standard. In addition to the external mechanical load, the wheel model is subjected to an internal load caused by the press-fitting of the wheel onto the axle. The wheel/axle interface for the numerical simulation is the average allowable overlap according to the geometric tolerances on the wheel and axle.

A 2D axisymmetric model was developed for thermal analysis using 5,072 quadratic elements. This model treated the material as isotropic elastoplastic with multilinear kinematic hardening. The material properties are determined through static tensile tests and insights from previous simulations, taking into account various temperatures that correspond to the operating conditions of the train wheel. All material properties are temperature-dependent. Fig. 8 shows boundary conditions for the thermal simulations. The boundary conditions for the thermal model were established to mimic the braking cycle based on testing conducted on a brake bench. This involved a 45-minute (2,700 seconds) braking period, generating heat and several hours of cooling to room temperature. Heat flux was applied at the wheel tread, where interaction with the braking blocks occurs, and convection was utilised across the wheel surface to accurately model the heat dissipation process. Three braking cycles were considered in one numerical simulation to obtain saturated values from the third simulated breaking cycle. The total simulation timed was 62,142 seconds. All results from thermal numerical simulations are obtained from the third breaking cycle.

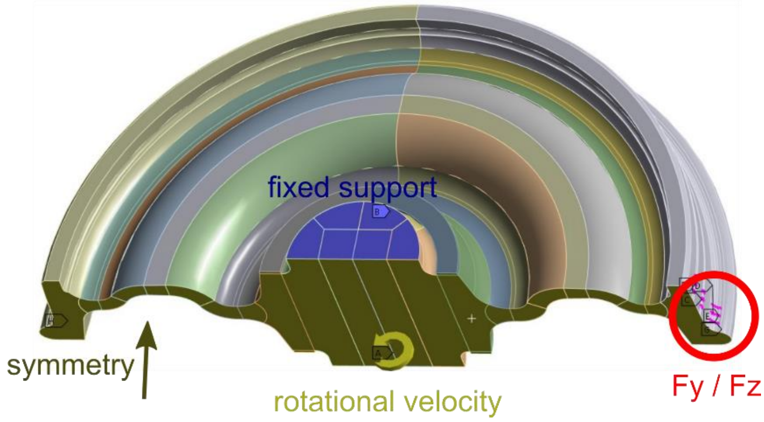

Fig. 7 Boundary conditions for the numerical model of mechanical wheel loading

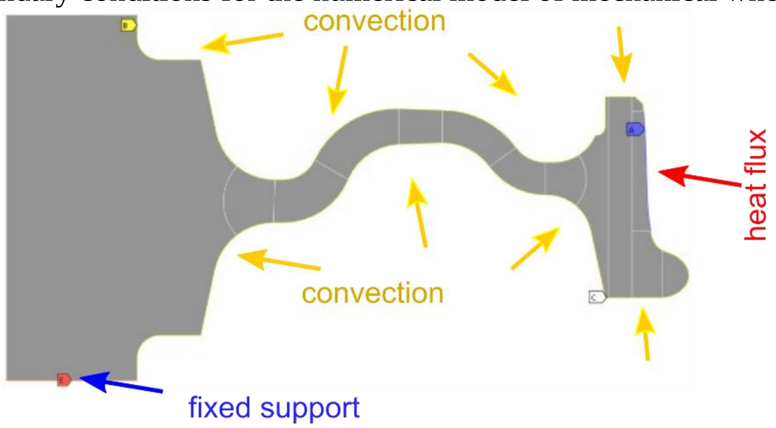

Fig. 8 Boundary conditions in numerical simulation for studying wheel braking cycles.

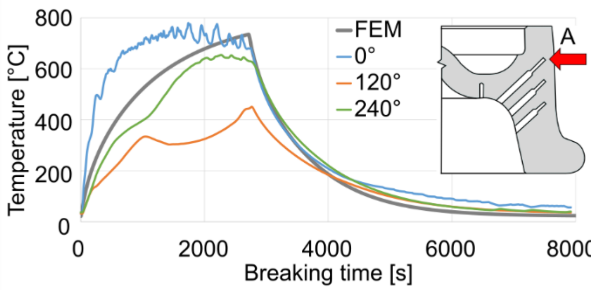

a) position A near the rail-wheel contact surface

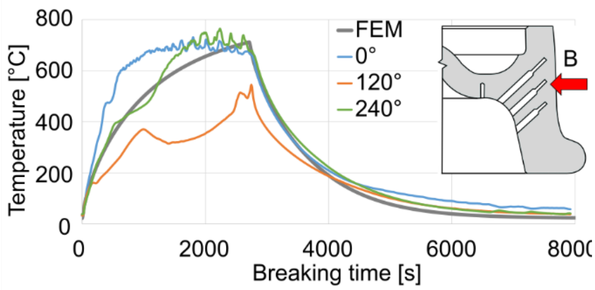

b) position B near the rail-wheel contact surface

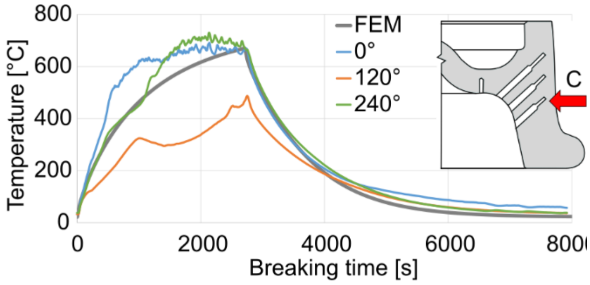

c) position C near the rail-wheel contact surface

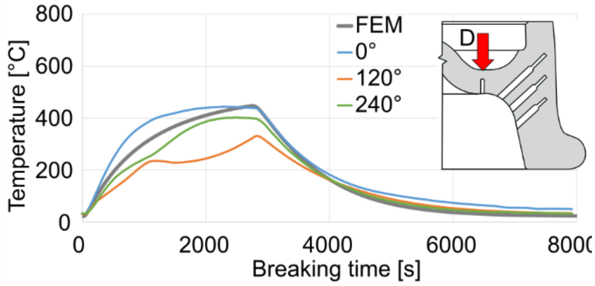

d) position D in the wheel web area

Fig. 9 Comparison of temperatures from numerical simulations and temperatures at individual thermocouples during the braking cycle for different thermocouple positions

The thermal numerical results were compared to experimentally measured temperatures during the braking test. Twelve temperature gauges were installed on the wheel, positioned at three different angular locations, spaced 120° apart, and at four points along the wheel cross-section. Fig. 9 shows the distribution of the experimentally measured and numerically simulated temperatures. The red arrows indicate the position of a temperature gauge on the wheel cross-section, while the different lines correspond to different angular positions. The black line represents results from numerical simulations.

For all gauge positions, the temperature increases as the braking cycle begins. For gauges near the braking surface, the temperature rises to approximately 700 °C within 1,500 seconds (25 minutes) and remains constant until braking ends. After braking ends, the wheel cools down rapidly, with the cooling rate slowing as the temperature drops toward room temperature. The temperature follows a similar trend for gauges in the wheel web, but the maximum temperature reaches only about 450 °C.

Temperatures determined at the 120° angular position are generally lower than those at 0° and 240°, attributed to wear on the braking surface, leading to an asymmetrical temperature distribution. Overall, the numerical simulations closely match the experimental data, validating the accuracy of the thermal numerical simulations.

5 Results

The development of the mechanical model allowed for a detailed examination of loading conditions for the different tracks. When considering von Mises stress, mechanical simulations do not indicate any critical locations in the wheel web area, as the determined stress for each track type remains below the fatigue limit. The fatigue limit for R73 steel at room temperature is 250 MPa. Fig. 10 illustrates the von Mises stress distribution for different sections of tracks, with the maximum stress highlighted in the wheel web area. It is important to note that the highest stress is located where the load is applied. However, this numerical simulation type is unsuitable for investigating rolling contact fatigue, which primarily occurs in the rail-wheel contact area. Therefore, thermal numerical simulations are employed to investigate what happens during braking. Radial stress acts as dominant for damage accumulation, further presented in the following text. Fig. 11 shows radial stress distribution for the cross-section of the wheel after the braking cycle when the wheel cools down to room temperature. High-stress gradients occur because of plasticisation during the braking due to temperature and rising stress. Red arrow shows the maximal radial residual stress. This position is investigated further to demonstrate stress behaviour during braking.

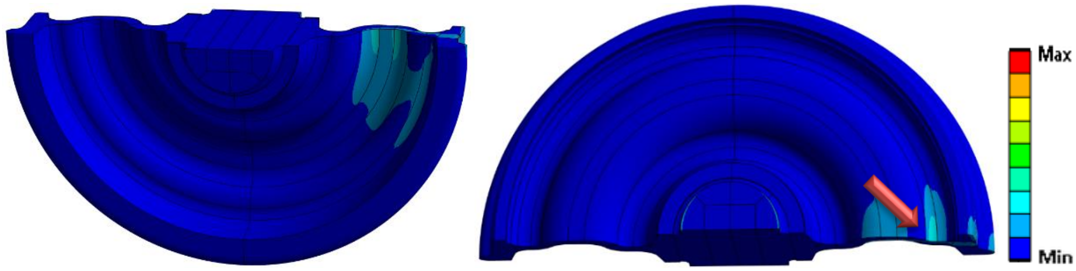

a) straight section of track

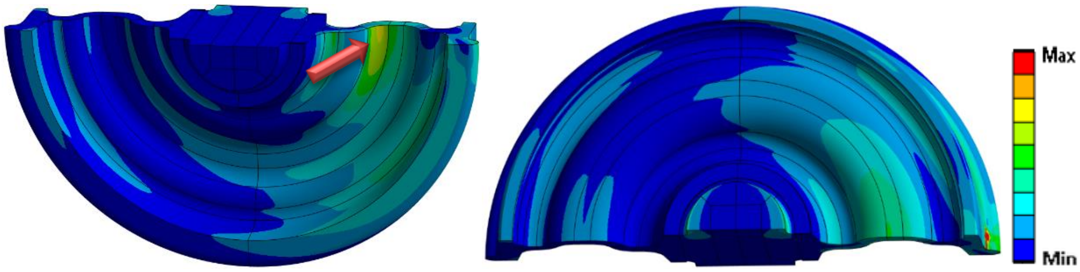

b) curved section of track

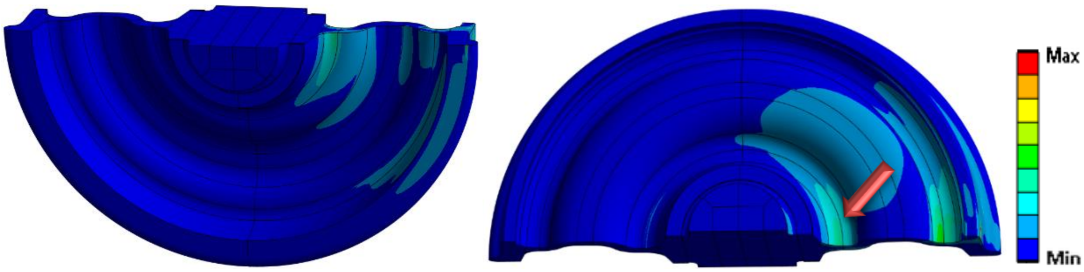

c) turnout

Fig. 10 Von Mises equivalent stress for the train ride according to different sections of track with marked wheel web maximum stress (only mechanical load); a) straight rail; b) curved rail; c) turnout

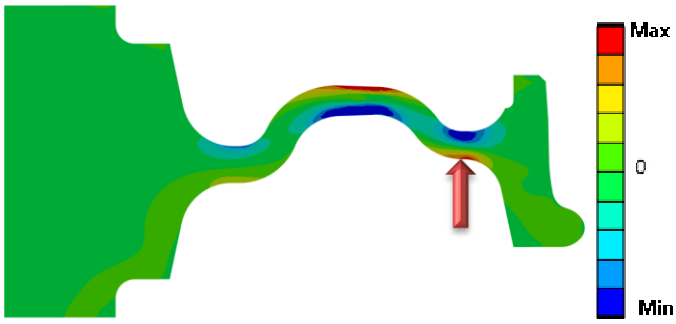

Fig. 11 Radial (X direction) residual stress distribution at room temperature after the braking cycle

Fig. 12 shows radial stress (blue dots; left axis) and temperature (orange dots; right axis) behaviour during the braking. The graph shows that the positive radial stress values transition to negative during the braking cycle. A similar, but reversed, pattern can be observed at other locations on the wheel. This shift defines a new stress cycle caused by the heat generated during braking. Fig. 12 also highlights the maximum temperature of 440 °C, reached at the end of braking. Initially, the radial stress is at its peak value of 400 MPa at room temperature. However, it rapidly decreases to the lowest of -280 MPa at 334 °C, approximately 1,087 seconds (around 18 minutes) after braking starts. Following this drop, the stress gradually increases due to stress redistribution in the surrounding material after the plasticisation. Due to the decrease in yield stress (after the temperature rises), the radial stress slowly increases. When braking ends, there is another rapid shift in stress, with radial stress rising back to its maximum value as the wheel returns to room temperature, showcasing the complex interplay between thermal effects and material stress responses during braking cycles.

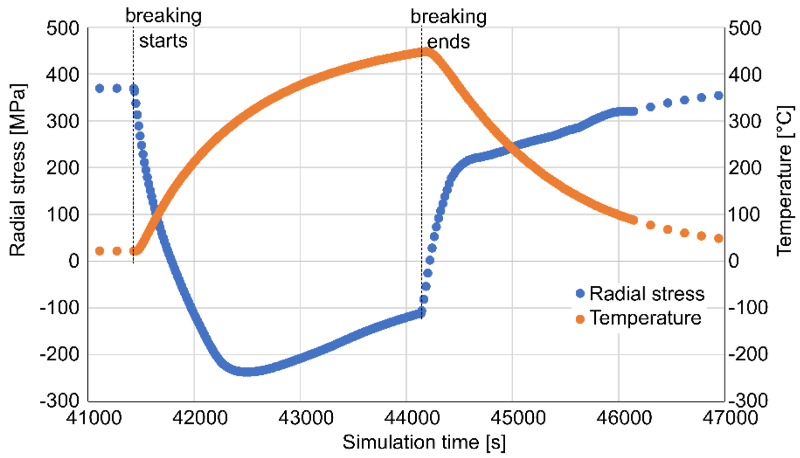

Fig. 12 Radial stress and temperature evolution during the braking cycle of the marked position in Fig. 11

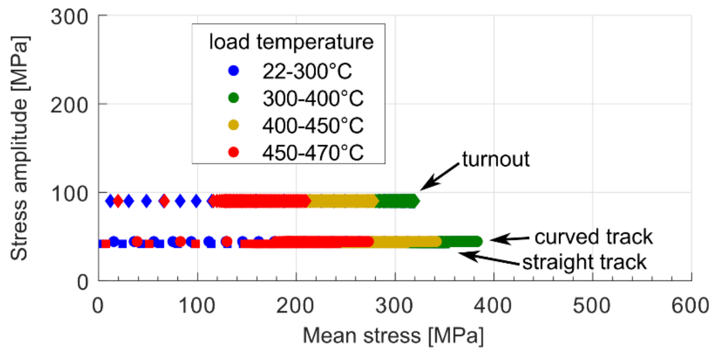

Fig. 13 The combination of mechanical (stress amplitude) and thermal loading (mean stress) for various temperatures in the investigated area; see red arrow in Fig. 11

Thermal analysis provides insights into the mean stress experienced during loading cycles and the temperature distribution that alters material properties, including yield stress and fatigue limit. From mechanical analysis, we derive amplitudes and adjustments to mean stress, which allow us to compile overall loading cycles for various rail track conditions. Complete new critical areas are obtained with the superposition of thermal simulations and the mechanical simulation results. One way to evaluate the critical areas with changing mean stress is to construct a Haigh diagram. Fig. 13 shows Haigh-like diagram points constructed from numerical results for different track sections for different temperatures with mean stress variating during the braking. Experimental fatigue limits should be determined for various temperatures and mean stress to evaluate the Haigh diagram correctly.

CONCLUSION

The paper investigates fatigue damage in the wheel web area of the railway wheel, where some cracks were previously revealed after service operation. The mechanical simulations performed according to valid standards cannot reliably predict critical areas. Therefore, additional thermal simulations were performed, and new critical areas were observed. The microstructural analysis of the wheel cross-section showed no significant changes in the wheel web area, even after the breaking. Therefore, homogenous material can be considered for mechanical and thermal numerical simulations.

By merging the numerical outcomes of both mechanical and thermal analyses, it becomes possible to construct the loading cycle for a railway wheel. Nevertheless, to ensure the accuracy of these numerical models, their validation against experimental data is crucial. This process requires collecting substantial experimental data, especially since the mechanical properties of materials change with temperature. Therefore, it is necessary to acquire experimental data such as Wöhler curves at various temperatures and under different loading asymmetries.

Following thorough experimental testing, it is possible to create the Haigh diagram. This diagram illustrates the fatigue limit for different stress amplitude and the mean stress. Consequently, pinpointing critical areas within the railway wheel web for potential failure is a complex task that requires sophisticated numerical modelling.

ACKNOWLEDGEMENTS

This research has been supported by grant No. FW03010149 "New wheel design for freight transport with higher utility properties" of The Technology Agency of the Czech Republic.

REFERENCES

[1] Žiaran, S., Šooš, Ľ., Chlebo, O. "Monitoring of Machinery Components During Their Life Cycle", Strojnícky časopis – Journal of Mechanical Engineering 74(1), pp. 181 – 190, **2024**. DOI: 10.2478/scjme-2024-0018

[2] Asplund, M., Palo, M., Famurewa, S., Rantatalo, M. "A study of railway wheel profile parameters used as indicators of an increased risk of wheel defects", Proceedings of the Institution of Mechanical Engineers, Part F: Journal of Rail and Rapid Transit. 230 (2), pp. 323 – 334, **2016**. DOI: 10.1177/0954409714541953

[3] Steyn, E. "Railway wheel steel behaviour upon thermo-mechanical loadings", B.m., Chalmers University of Technology, **2022**. Available at: https://research.chalmers.se/publication/532338/file/532338_Fulltext.pdf

[4] Alemi, A. "Railway wheel defect identification", B.m., Delft University of Technology, **2019**. DOI: 10.4233/uuid:981edd2c-1674-4cba-8146-cf097b29c4f1

[5] Dick, M., Sundaram, N., Sherrock, E. "Wheel Failure Investigation Program: Phase I", Federal Railroad Administration, Washington DC, **2021**. Available at: https://railroads.dot.gov/sites/fra.dot.gov/files/2021-02/Wheel%20Failure%20Investigation%20Program%20Phase%20I.pdf

[6] Sofer, M., Fajkoš, R., Halama, R. "Influence of induction hardening on wear resistance in case of rolling contact", Strojnícky časopis – Journal of Mechanical Engineering 66 (1), pp. 17 – 26, **2016**. DOI:10.1515/scjme-2016-0007

[7] EN 13979-1, "Railway applications - Wheelsets and bogies - Monobloc Wheels - Technical approval procedure - Part 1: Forged and rolled wheels", **2020**.

[8] Suetrong, C., Uthaisangsuk, V. "Investigations of fatigue crack propagation in ER8 railway wheel steel with varying microstructures", Materials Science and Engineering: A. 840 (March), 142980, **2022**. DOI: 10.1016/j.msea.2022.142980

[9] Vakkalagadda, M. R. K., Vineesh, K. P. "Causes and failure forms of railway wheels", Materials Today: Proceedings. 98 (July 2023), pp. 97 – 101, **2024**. DOI: 10.1016/j.matpr.2023.09.161

[10] Mráziková, L., Lauschmann, H. "Quantitative fractographic analysis of impact fracture surfaces of steel R73", Strength of Materials 40 (1), pp. 67 – 70, **2008**. DOI: 10.1007/s11223-008-0018-8

[11] Dick, M., Sundaram, N., Sherrock, E. "Wheel Failure Investigation Program: Phase II". Federal Railroad Administration, Washington DC, **2021**. Available at: https://railroads.dot.gov/sites/fra.dot.gov/files/2021-12/Wheel%20Failure%20Investigation%20Phase%202.pdf

[12] Cummings, S. "Broken Rims in Railroad Wheels", Federal Railroad Administration, Washington DC, **2014**. Available at: https://railroads.dot.gov/sites/fra.dot.gov/files/fra_net/14325/Broken%20Rims%20in%20Railroad%20Wheels_final.pdf